A Modular Optimal Estimation Method for Combined Radar–Radiometer Precipitation Profiling

S. JOSEPH MUNCHAK AND CHRISTIAN D. KUMMEROW

Department of Atmospheric Science, Colorado State University, Fort Collins, Colorado

ABSTRACT

Although zonal mean rain rates from the Tropical Rainfall Measuring Mission (TRMM) are in good (<10%) agreement between the TRMM Microwave Imager (TMI) and precipitation radar (PR) rainfall algorithms, significant uncertainties remain in some regions where these estimates differ by as much as 30% over the period of record. Previous comparisons of these algorithms with ground validation (GV) rainfall have shown significant (>10%) biases of differing sign at various GV locations. Reducing these biases is important in the context of developing a database of cloud profiles for passive microwave retrievals that is based upon the PR-measured profiles. A retrieval framework based upon optimal estimation theory is proposed wherein three parameters describing the raindrop size distribution (DSD), ice particle size distribution, and cloud water path (cLWP) are retrieved for each radar profile. The modular nature of the framework provides the opportunity to test the sensitivity of the retrieval to the inclusion of different measurements, retrieved parameters, and models for microwave scattering properties of hydrometeors. The retrieved rainfall rate is found to be strongly sensitive to the a priori constraints in DSD and cLWP; thus, these parameters are tuned to match polarimetric radar estimates of rainfall near Kwajalein, Republic of Marshall Islands. An independent validation against gauge-tuned radar rainfall estimates at Melbourne, Florida, shows agreement within 2%, which exceeds previous algorithms' ability to match rainfall at these two sites. Errors between observed and simulated brightness temperatures are reduced and climatological features of the DSD, as measured by disdrometers at these two locations, are also reproduced in the output of the combined algorithm.

1. Introduction

Global measurements of precipitation have been made possible over the past two decades by increasingly sophisticated technology available on satellite platforms. Although infrared (IR) techniques had been in use since the advent of geostationary satellites (Barrett 1970), the relationship between IR brightness temperatures T_b and surface rainfall is rather tenuous. More reliable satellite precipitation estimates were achieved in 1987 with the launch of the Special Sensor Microwave Imager (SSM/I) on the polar-orbiting Defense Meteorological Satellite Program *F8* (Hollinger et al. 1990). At lower microwave frequencies (e.g., 19 GHz), the emission from precipitating clouds over oceans appears radiometrically warm compared to the background. This "warmth" is strongly related to the column-integrated liquid water. At higher frequencies (e.g., 85 GHz), the emission signal saturates at smaller amounts of liquid water, but increasingly effective scattering by precipitation-size ice crystals creates a T_b depression. Both of these signatures are physically related to the hydrometeor profile but contain limited information. Algorithms that seek to retrieve the surface rain rate from microwave observations often rely on Bayesian schemes that involve a database of cloud and precipitation profiles (Kummerow and Giglio 1994; Kummerow et al. 2001).

Another major milestone was reached in 1997 with the launch of the Tropical Rainfall Measuring Mission (TRMM). In addition to a microwave radiometer [TRMM Microwave Imager (TMI)], the platform included the first spaceborne precipitation radar (PR). In addition to its higher spatial resolution, the PR measures the vertical profile of precipitation. Rainfall measurements from both instruments have shortcomings, which can be attributed to their sensitivity to different geophysical parameters related to rainfall as well as assumptions inherent in the algorithms

Corresponding author address: S. Joseph Munchak, Department of Atmospheric Science, Colorado State University, 1371 Campus Delivery, Fort Collins, CO 80523-1371.
E-mail: jmunchak@atmos.colostate.edu

used to retrieve rainfall from T_b or reflectivity measurements. A global comparison of PR and TMI rainfall retrievals reveals distinct regional biases (Berg et al. 2006). It has been suggested that these may be a result of differences between the instruments' threshold sensitivity to shallow and/or light rainfall (Shimizu et al. 2009), errors in assumptions about the raindrop size distribution (DSD) in the radar algorithm (Iguchi et al. 2009; Kozu et al. 2009), or systematic biases in the database that is the foundation for radiometer-based retrievals (Seo et al. 2007).

Notwithstanding these inconsistencies, the TRMM data have provided unique insight into the tropical hydrologic cycle and its response to short-term variability such as the El Niño–Southern Oscillation (ENSO) and the Madden–Julian oscillation (MJO) (e.g., L'Ecuyer and Stephens 2007; Chen et al. 2007; Masunaga et al. 2006; Morita et al. 2006; Cho et al. 2004). However, longer-term trends are more difficult to discern, in part because of these discrepancies between retrievals. One of the most pressing questions surrounding climate change is the rate at which precipitation scales with water vapor in the atmosphere. Held and Soden (2006) reviewed the projections from the suite of climate models included in the Fourth Assessment Report of the Intergovernmental Panel on Climate Change, and noted that, while water vapor scales at a rate near 7% K^{-1}, precipitation scales at a reduced rate near 2% K^{-1}. This predicted scaling is consistent with the energy budget analysis of Allen and Ingram (2002). However, Wentz et al. (2007) observe that in the 20-year record of precipitation derived from SSM/I instruments, which closely resembles the TMI record during coincident time–space subsets owing to their similar physical basis and algorithm, precipitation and evaporation scale at the same rate as water vapor. Interestingly, Berg et al. (2006) found that the ratio of TMI to PR rain rate was greatest in regions with high values (>3 g cm^{-2}) of column-integrated water vapor, and suggested that these differences may be due to incorrect assumptions about cloud properties in higher vapor environments. If there is a positive bias in radiometer-only precipitation in high water vapor regimes, then the observed precipitation–water vapor scaling relationship may be artificial. This underscores the importance of resolving the differences between radar and radiometer estimates of precipitation, and in particular understanding the relationship between the environmental water vapor and cloud properties.

To address these issues, a retrieval framework that incorporates both PR and TMI measurements to retrieve a set of consistent geophysical parameters has been developed. Although the theory for multimeasurement retrievals has been reasonably well established (Rodgers 2000), a problem posed by the multi-instrument data

provided by TRMM and other platforms such as the A-Train (Stephens et al. 2002) lies in the greatly differing resolutions and mismatched instrument fields-of-view (FOVs), especially where the FOVs are significantly larger than the scale of the features being retrieved. A number of different techniques have been proposed to deal with these issues, particularly in the context of TMI + PR combined retrievals.

The initial operational combined algorithm for TRMM (Haddad et al. 1997) adjusts the radar-estimated path-integrated attenuation (PIA), upon which the rain DSD is based, via empirical relation to the extinction measured in the 10-GHz channel. In this algorithm, each PR pixel was sensitive to the 4 nearest TMI 10-GHz FOVs and a Bayesian approach was used to adjust the radar-derived rain profiles in the intersection of these 4 footprints to match the observed brightness temperatures. More recently, algorithms have been developed to utilize information from all TMI channels to enhance the PR retrieval and to generate databases to be used in passive-only retrievals. Grecu et al. (2004) and Masunaga and Kummerow (2005) independently developed methodologies to match PR observations to a database of hydrometeor profiles generated from cloud-resolving models (CRMs). Brightness temperatures are then simulated from these profiles and convolved to the TMI channel FOVs. In both of these algorithms, an adjustment is made to the DSD in the hydrometeor profile to simultaneously match the TMI-observed brightness temperatures; however, the methodologies differ in how these adjustments are made.

Masunaga and Kummerow (2005) developed a technique primarily intended to adjust the CRM databases of raining profiles and associated brightness temperatures to be used in passive-only retrievals. Initial profiles were selected based upon similarities in the observed and CRM reflectivity profiles and T_bs were computed from the modeled profiles at the PR resolution. The modeled T_bs were then convolved to the TMI resolution and compared to observed T_bs that were interpolated at each pixel. Thus, the adjustment made to the DSD to account for the difference in observed and modeled brightness temperature is done independently for each PR pixel. A shortcoming of this method is the implicit assumption that each PR pixel within a given TMI FOV is equally responsible for the difference in observed and modeled brightness temperature. This assumption may not be valid for scenes with a significant variability in rainfall physics within an FOV.

Grecu et al. (2004) formulated a retrieval that modified a parameter of the DSD in the hydrometeor profiles. The initial profiles were derived by matching reflectivities to a CRM database, similar to Masunaga and Kummerow (2005). Unlike their retrieval, however, Grecu et al.

(2004) perform the retrieval on multiple TMI FOVs and PR profiles simultaneously because of the overlapping nature of the TMI FOVs. Their retrieval minimized a cost function consisting of three terms: the difference between observed and modeled values of an index related to brightness temperature, the deviation of the modified DSD parameter from its spatial average, and difference between the radar-estimated and modeled PIA. All of the terms in the cost function are weighted by covariances which represent the expected deviation between observed and modeled values, and mostly represent uncertainties in nonretrieved parameters that nevertheless are necessary to perform the radiative transfer calculations. The authors noted that the values of covariances were somewhat uncertain, and performed an analysis showing that the retrieval was rather sensitive to their magnitudes. Thus a more precise estimate of these errors, or a formulation that is less sensitive to their relative magnitudes, is desirable for increased confidence in the retrieved precipitation estimates.

In this study, we use a variational optimal estimation inversion (Rodgers 2000) embedded within a modular framework to retrieve rainfall profiles that are consistent with all available observations (radar reflectivity, radar PIA, TMI T_bs). This method differs from existing algorithms in the following ways:

- three parameters describing the rain DSD, ice particle size distribution (PSD), and cloud water are retrieved for each radar pixel [previous algorithms only retrieve the DSD and, in the case of Masunaga and Kummerow (2005), ice density];
- brightness temperatures are incorporated directly [as opposed to the indices used by Grecu et al. (2004)] and at their native resolution [instead of the interpolation used by Haddad et al. (1997) and Masunaga and Kummerow (2005)];
- the influence of nonraining parameters in FOVs with partial rain coverage is explicitly handled with a nonraining retrieval scheme; and
- an a priori covariance matrix is defined to constrain the retrieval results, including spatial structures [this was not included in Grecu et al. (2004) and is not applicable to the other methods].

The algorithm details are described in section 2 including a sensitivity and information content analysis. The partitioning of rain and cloud water constitutes a free parameter in this formulation and section 3 describes how we used TRMM Ground Validation products at Kwajalein and Melbourne, Florida, to adjust and independently validate this partitioning. Section 3 also includes comparisons of simulated and observed T_bs and comparison of the retrieval results with disdrometer DSD measurements. A summary is presented in section 4.

2. Retrieval methodology

A brief outline of the relevant aspects of optimal estimation theory is given in this section, followed by a detailed description of the radar profiling algorithm. The incorporation of this algorithm into the larger framework of the combined retrieval follows. This section closes with an analysis of the information added to the radar-based retrieval by the TMI observations.

a. Optimal estimation theory

Optimal estimation (OE) is an inversion method that has been devised for retrieving a set of parameters **x**, which represent the true state of the system being observed, from a set of measurements **y** that are related through a forward model, $\mathbf{y} = f(\mathbf{x})$. This methodology is described in detail by Rodgers (2000); a brief summary is presented here. Optimal estimation seeks to find the set of parameters $\hat{\mathbf{X}}$ that minimizes the cost function

$$\Phi = [\mathbf{y} - f(\hat{\mathbf{X}})]^{\mathrm{T}} \mathbf{S_y}^{-1} [\mathbf{y} - f(\hat{\mathbf{X}})] + (\hat{\mathbf{X}} - \mathbf{x}_a)^{\mathrm{T}} \mathbf{S}_a^{-1} (\hat{\mathbf{X}} - \mathbf{x}_a),$$

(1)

where $\mathbf{S_y}$ is the measurement covariance matrix. This cost function differs slightly from that of Grecu et al. (2004) in the inclusion of $\mathbf{x}_a$, the a priori parameter set, and its covariance matrix $\mathbf{S}_a$. Without $\mathbf{x}_a$, the solution only minimizes the variance in the observations and can be underconstrained. The a priori parameter set represents the expected value of the retrieved parameters absent any information from the measurement and prevents extreme, unphysical values from being retrieved. Thus, the two terms in the cost function represent the weighted differences between the measurements and retrieved parameters from their forward-modeled and expected values, respectively. The relative weighting of these two terms that can substantially influence the location of the minimum cost, thus we describe the covariance matrices in more detail in section 2c. The diagonal elements in these matrices contain the variances of the elements of $\mathbf{x}_a$ and **y**. The off-diagonal elements represent the covariances between different measurements or the retrieval parameters. Nonzero values reduce the cost function if structures in the measurement or retrieval fields resemble those implied by the covariance matrices.

The solution that minimizes the cost function can be calculated iteratively if the forward model is moderately nonlinear, as is the case for radiative transfer. In each iteration, the forward model is linearized by calculating the Jacobian **K**, where $K_{ij} = \partial y_i / \partial x_j$. Then, Newton's method can be used to arrive at a solution once a convergence condition is satisfied. The iterative step is defined as

$$\hat{\mathbf{X}}_{n+1} = \hat{\mathbf{X}}_n + [(\mathbf{S}_a^{-1} + \mathbf{K}_n^{\mathrm{T}}\mathbf{S_y}^{-1}\mathbf{K}_n)^{-1}]\{\mathbf{S}_a^{-1}(\mathbf{X}_a - \hat{\mathbf{X}}_n)$$
$$+ \mathbf{K}_n^{\mathrm{T}}\mathbf{S_y}^{-1}[\mathbf{y} - F(\hat{\mathbf{X}}_n)]\}. \qquad (2)$$

The convergence criterion is usually defined in terms of the closeness of subsequent iterations. One such criterion is that the standardized change in $\hat{\mathbf{X}}$ from one iteration to the next is much less than the number of retrieved parameters N:

$$(\hat{\mathbf{X}}_{n+1} - \hat{\mathbf{X}})^{\mathrm{T}}(\mathbf{S}_a^{-1} + \mathbf{K}_n^{\mathrm{T}}\mathbf{S_y}^{-1}\mathbf{K}_n)^{-1}(\hat{\mathbf{X}}_{n+1} - \hat{\mathbf{X}}) \ll N. \qquad (3)$$

b. Radar profiling algorithm

To apply OE theory to a radar–radiometer combined retrieval, one must first choose the parameters that compose **x**. Our retrieval begins with a radar-only solution, and then adjusts that solution with the additional information provided by TMI. The radar-only solution is provided by a rainfall profiling algorithm, similar conceptually to the TRMM operational radar rainfall algorithm (2A25). To convert the profile of radar reflectivity into a rain rate near the surface at the PR frequency, this algorithm needs to correct for attenuation. Although the full details of the stand-alone 2A25 algorithm are covered in great detail by Iguchi et al. (2000, 2009), it is necessary to understand the assumptions required by such an algorithm so they are reviewed briefly here.

An attenuation-correcting radar algorithm was described by Hitschfield and Bordan (1954) using internally consistent relationships between reflectivity Z, hydrometeor content W, and attenuation k to retrieve hydrometeor profiles. This method is numerically unstable; that is, small changes in the $Z-k$ relationship can lead to large differences in the surface rain rate as errors in attenuation estimates amplify toward the surface. However, independent measurements of PIA provided by the surface reference technique (SRT; Meneghini et al. 2000) can provide a constraint on the $Z-k$ relationship or the DSD model used to derive it.

Before describing the vertical hydrometeor model, it is worth noting that a potential source of error is the detection threshold of PR (17 dBZ). The 2A25 algorithm can afford to ignore this problem, since rain of this reflectivity has negligible attenuation, but may nevertheless contribute to a substantial fraction of the total LWP and is important for modeling microwave T_bs. Our algorithm fills the gaps in profiles by adding reflectivity at the lowest value measured by PR in each profile below the 17 dBZ threshold. This has a modest effect on simulated T_bs, with an increase of up to 5 K in the 37-GHz channel.

The vertical model of the precipitating cloud requires a description of hydrometeor phase, size distribution, ice density and morphology (Bennartz and Petty 2001), and melting layer structure (Olson et al. 2001) at each range gate in order to properly simulate radar reflectivity and upwelling microwave radiances. Because of the computational cost of retrieving multiple variables in each profile, our radar profiling algorithm is designed to capture the natural variability of these properties in as few parameters as possible.

As in many other rain profiling algorithms [e.g., TRMM 2A25 (Iguchi et al. 2000); Grecu and Anagnostou 2002], a gamma distribution is assumed to describe the rain DSD: $N(D) = N_0 D^\mu e^{-\Lambda D}$, with an intercept parameter (N_0), shape parameter (μ), and slope parameter (Λ). In this model, the median volume diameter D_0 can be expressed as $D_0 = (3.67 + \mu)/\Lambda$ (Ulbrich 1983). This relationship formulates a power law relating D_0 and Z:

$$D_0 = (3.67 + \mu)\{[N_0\Gamma(7 + \mu)]^{-1}Z\}^{1/(7+\mu)}. \qquad (4)$$

The constants can be grouped together to form a more simple power law $D_0 = aZ^b$, where a represents the Z-normalized D_0 and is dependent on N_0 and μ, whereas b only depends on μ. It should be noted that these relationships are only strictly valid if Z represents the sixth moment, that is, Rayleigh reflectivity, which is not true for large raindrops (>1-mm diameter) at the PR frequency. However, the error introduced by this approximation does not significantly affect the shape of the relationship, so no systematic error is introduced so long as N_0 and D_0 are derived from PR reflectivity values using Mie theory to calculate Z. To simplify the retrieval, the coefficients a and b are fixed by rain type (Table 1) and, along with the assumption $\mu = 3$, are chosen to approximate the 2A25 default $Z-R$ relationships.

To adjust the $Z-D_0$ relationship (e.g., in order to match the SRT PIA), we define a multiplicative factor ϵ_{DSD}, so that $D_0 = \epsilon_{\mathrm{DSD}}aZ^b$. This type of DSD adjustment is mathematically similar to the δN_0^* adjustment employed by Grecu and Anagnostou (2002) in their profiling algorithm and the α adjustment employed by 2A25 (Iguchi et al. 2000).

The ice phase is treated similarly. An exponential size distribution (i.e., $\mu = 0$) is assumed for both snow and graupel above the melting layer, which is consistent with available aircraft measurements (e.g., Houze et al. 1979; Stith et al. 2002). The following size–density relationships for snow (ρ_s) and graupel (ρ_g), based on Heymsfield et al. (2004) are assumed:

$$\rho_s = 128D^{-0.95} \quad \text{and} \qquad (5)$$

$$\rho_g = 96D^{-0.95}, \qquad (6)$$

TABLE 1. Default PSD parameters by 2A23 rain type.

Parameter	Convective–other	Stratiform
a_{rain}	0.4778	0.5973
b_{rain}	0.1210	0.1073
a_{snow}	1.85	1.85
a_{graupel}	0.31	0.31
b_{snow}	0.16	0.16
b_{graupel}	0.16	0.16

where D is in millimeters and density is in kilograms per meter cubed and is not allowed to exceed the density of pure ice. The snow–graupel partitioning is assumed to be a function of temperature and rain type (Fig. 1) and derived from the database of CRM simulations used in radiometer-only retrievals (Kummerow et al. 2001). Improving the microphysics schemes in these simulations is an active area of research (e.g., Li et al. 2008) and part of planned prelaunch Global Precipitation Measurement (GPM) ground validation.

As with rain, a $Z-D_0$ power law ($D_0 = aZ^b$, where D_0 represents the mass-weighted average diameter of snow and graupel) is used to derive the ice PSD from the corrected reflectivity. From this PSD, the attenuation and scattering properties at all TMI frequencies can be calculated. In this study, the equivalent-mass sphere approach has been used to calculate the scattering properties of snow and graupel. This assumption can lead to significant errors in the scattering and extinction parameters for a given ice water content (Petty and Huang 2010), on the order of the difference between an all-snow and all-graupel column of the same reflectivity. Despite these numerous sources of error, there is minimal impact on the retrieved rainfall because attenuation at radar and lower TMI frequencies is insignificant (<0.01 dB km^{-1} for 1 g m^{-3} at 13.8 GHz). The parameters of the $Z-D_0$ relationships for rain, snow and graupel are given in Table 1 and are consistent with the Z–ice water content (IWC) relationships reported by Black (1990). Like the rain DSD, these can be adjusted by a multiplicative factor, which we define as ϵ_{ICE}. This has the effect of increasing or decreasing the ice water path, for example, to match the scattering signature at 85 GHz.

Our melting layer model is based on the finding of Zawadzki et al. (2005) that the strength of the reflectivity peak is strongly related to the density of the melting ice particles. Our treatment begins by finding the peak corrected (2A25) reflectivity (Z_{peak}) within 0.5 km of the horizontally interpolated brightband height, provided by the standard TRMM 2A23 product. The brightband strength is given by the difference between Z_{peak} and the lowest 2A25 reflectivity within 1 km below Z_{peak} and is used to determine the initial snow density at the top of the
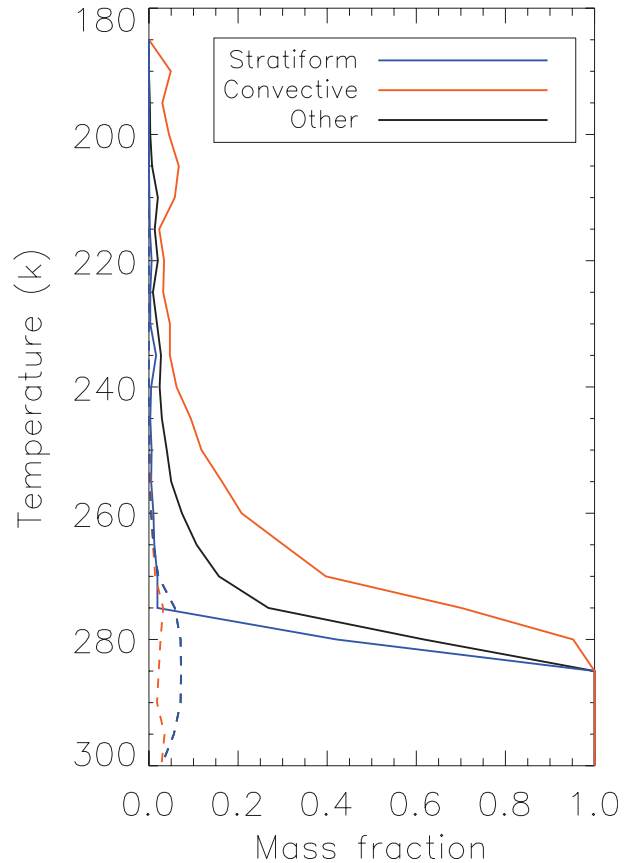

FIG. 1. Default profiles of graupel (solid) and cloud water (dashed).

melting layer. For a given density, there is a relationship between melt fraction and $Z_{\text{peak}} - Z$ (Fig. 2), which is used to determine the dielectric constant and fall velocity ratio at levels up to 0.5 km above and 1 km below Z_{peak}. With this additional information, the PSD is derived using the same μ and $Z-D_0$ relationship as the rain, ensuring continuity between the melting and rain layers.

Although this model does not account for coalescence and breakup, these processes lead to errors of only 1 dB (Fabry and Zawadzki 1995), only slightly more than the noise in the radar itself. This approach has the advantage of mass consistency from top to bottom of the layer, which is an improvement over static $Z-R$ and $Z-k$ relationships in the melting layer, which are not valid at all densities. Furthermore, there is no need for explicitly separate convective and stratiform melting layer models since a weak Z_{peak} implies high particle density, that is, graupel, whereas a stronger value is associated with lower-density snow.

Cloud water has a small but nonnegligible contribution to attenuation at the PR frequency, and a stronger contribution to T_bs, especially at higher frequencies and
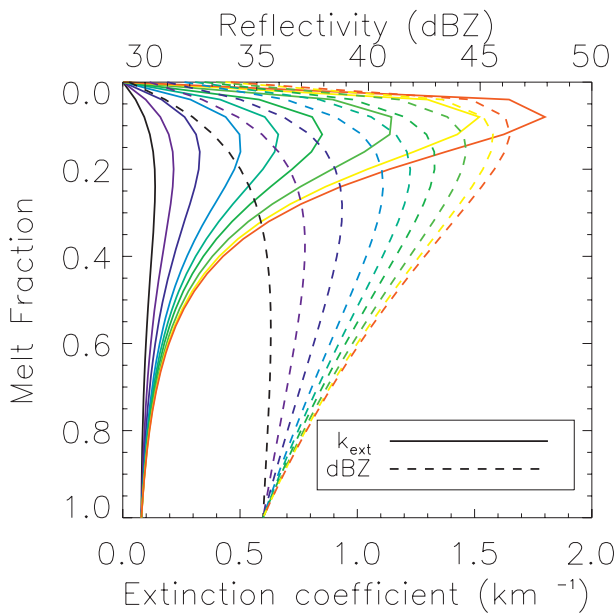
FIG. 2. Profiles of the 13.8-GHz extinction coefficient and reflectivity for a sample distribution of melting particles. Density decreases going from black to red; values are 50, 67, 100, 150, 200, 267, 400, 567, and 800 kg m^{-3}.

TABLE 2. Summary of retrieval parameters.

Parameter	Description
ϵ_{DSD}	Median raindrop size (D_0) divided by aZ^b
ϵ_{ICE}	Median ice particle size divided by aZ^b
ϵ_{CLW}	Multiplicative factor for default cloud water profile

the variance of the SRT, which is known, and the variance of ϵ_{DSD}, which has not been defined. When our profiling algorithm is used without radiometer input, we desire that the global rainfall estimates be unbiased relative to 2A25 both to serve as a standard reference to compare the radiometer-adjusted estimates and to indirectly utilize the data against which 2A25 itself has been validated. In this simple case, x consists of ϵ_{DSD} and **y** is the SRT PIA, with the profiling algorithm serving as the forward model to calculate the PIA from the measured Z profile (ϵ_{ICE} and ϵ_{CLW} are not considered in the radar-only retrieval because of their minimal impact upon the PIA). The only free parameter in this retrieval is the uncertainty in ϵ_{DSD}. An analysis of profiler-derived (Williams 2008) and polarimetric radar–derived (Matrosov et al. 2002) DSDs suggests a Z-normalized D_0 standard deviation of approximately 35%. One month of global retrievals over ocean provides a best match to 2A25 when 25% variance is assumed. Different variance levels in Fig. 3 illustrate the trade-off between matching the observations (SRT PIA) versus the constraint of the default DSD. When the constraint on the DSD is strong, it is difficult to adjust rain rates away from the default value, which tends to produce less rain than the standard 2A25 solution.

c. Combined retrieval framework

The flow of the overall retrieval is illustrated in Fig. 4. The parameters ϵ_{DSD}, ϵ_{ICE}, and ϵ_{CLW} required by the radar profiling algorithm form the retrieval vector x. In addition, there is another set of parameters that do not affect the radar solution but are necessary to model the T_bs. These parameters include SST and surface wind speed, which are necessary for emissivity calculations. Also, since most TMI FOVs cover some nonraining PR pixels, the cLWP, total precipitable water (TPW), and height of the freezing level need to be known for these pixels in order accurately model the microwave T_bs. These parameters are obtained either through ancillary sources or independent retrievals.

SSTs are derived from a multiday optimal interpolation (Reynolds and Smith 1994) of TMI-based SST retrievals (Gentemann et al. 2004). The SST data are gridded at 0.25° resolution, so a bilinear interpolation is used at each pixel. The freezing level at all PR pixels within 300 km of a reliable brightband height is interpolated using an
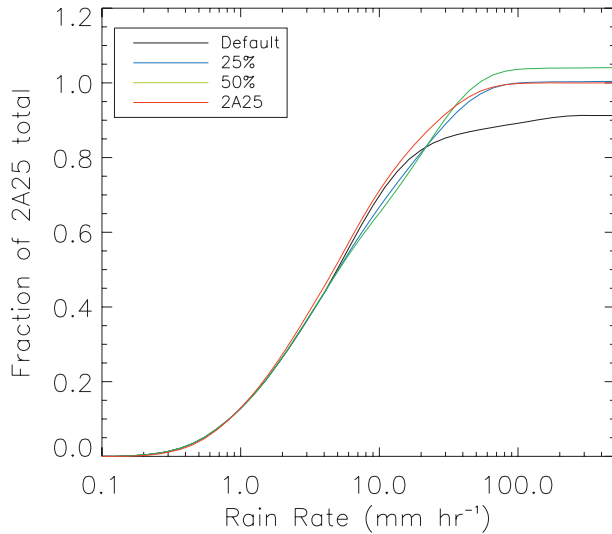
in lighter rain. Like the snow–graupel partitioning, default cloud water profiles are derived from the CRM database (Fig. 1) for each rain type. Since the cloud liquid water path (cLWP) makes an important contribution to microwave T_bs, particularly in light rain, we define a third adjustable parameter, ϵ_{CLW}, which is used to multiply the default cLWP equally at all levels in the combined retrieval algorithm.

In summary, the profiling algorithm converts the observed reflectivity profile into a profile of hydrometeor PSDs with three adjustable parameters: ϵ_{DSD}, ϵ_{ICE}, and ϵ_{CLW} (Table 2). From the top down, an attenuation correction is made at each range gate, the PSD is derived from the corrected reflectivity and ϵ values, and the process is repeated to the lowest clutter-free bin, below which the same DSD is extrapolated to the surface. This process is similar to 2A25, although there are differences in details of the ice, mixed phase, and cloud water models.

Perhaps the most important difference is in incorporation of the SRT PIA. Since the standard deviation of the SRT can be greater than the PIA estimate itself in light and even moderate rain, the profiling algorithm needs to account for this to prevent unphysical profiles from being retrieved. The 2A25 algorithm uses a combination of the default and SRT solution that gives higher weight to the SRT PIA in heavy rain, where the SRT is most reliable. With the OE methodology, the default and SRT solution can be weighted with knowledge of

FIG. 3. Rain CDFs over global ocean for January 2000 using different constraints on the default DSD.

FIG. 4. Flowchart of TRMM combined PR + TMI retrieval, illustrating the modular nature of the overall algorithm.

inverse distance scheme with smoothing from the top of the bright band as given by the 2A23 product (rain characteristics) where a bright band is detected. For pixels more than 1000 km from a reliable height, the climatological freezing height level used by 2A25 is given instead, and a linear combination is used in between 300 and 1000 km.

The surface wind, TPW, and cLWP are retrieved independently at each TMI FOV using the method of Elsaesser and Kummerow (2008) and interpolated to the nonraining PR pixels. This retrieval is considered valid where the χ^2 error statistic is less than 18, which is indicative of a homogeneous wind, TPW, and cloud water field with no precipitation. The temperature profile is calculated assuming a constant lapse rate that is calculated from the freezing height and SST (with a maximum of 7 K km^{-1}), and a scale height of 2.3 km is assumed for water vapor. In pixels with a radar echo, wind is interpolated as in the rain-free pixels, but the water vapor values are adjusted to 95% RH in range gates with an echo.

Since many of the TMI FOVs are only partially filled with raining PR pixels, it is necessary to have an accurate representation of the nonraining parameters outside the raining pixels. The chief cause of poor nonraining retrievals, aside from rain, is sub-FOV inhomogeneity of the cloud water field (Rapp et al. 2009) as well as contributions from drizzle, which has larger drops that create a different T$_b$ signature than cloud water, but are too small to be detected by PR. Thus, we retrieve the cloud + drizzle LWP for all nonraining PR pixels that were within 30 km (approximately the size of a 19-GHz FOV) of any TMI nonraining retrieval that did not meet
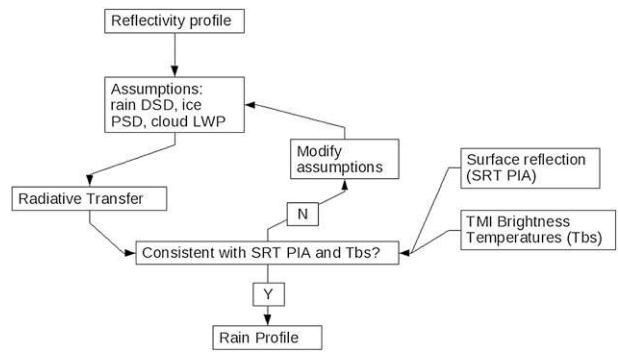
the $\chi^2 < 18$ test or are adjacent to a PR pixel with rain. Cloud is assumed to transition to drizzle once a LWP of 150 g m^{-2} is reached; this is based on a median value inferred from *CloudSat* and Moderate Resolution Imaging Spectroradiometer (MODIS) observations by Kubar et al. (2009). To maintain continuity among raining and nonraining pixels, the retrieved cloud LWP is interpolated into the raining pixels if it exceeds the value given by the default rainwater–cloud water relationships.

The next two routines retrieve the parameters used by the profiling algorithm (Table 2). Since modifying the ice PSD affects primarily the 85-GHz channels, where the emission signal is saturated even in light rain and therefore insensitive to cloud water–rain DSD modifications, this process is separated from the rain DSD and cloud water retrieval for computational efficiency. Rain and cloud water, on the other hand, must be retrieved simultaneously because of their similar, but not identical, contributions to upwelling microwave radiation at the TMI frequencies.

In each retrieval routine, the a priori covariance matrix $\mathbf{S}_a$ must be carefully constructed so that the algorithm can reproduce the variability observed in nature without giving unphysical profiles. To place an equal cost on any given increase–decrease of rain D_0, ice D_0, and cLWP, we assume the ϵ parameters are distributed lognormally. The variance of ϵ_{DSD} has already been established via matching to 2A25 and observations, but the covariance also needs to be defined, because the observational datasets (Matrosov et al. 2002; Williams 2008) used to determine the variance of ϵ_{DSD} also show spatial–temporal autocorrelation structure of the form

$$\mathbf{S}_a(i, j) = \mathbf{S}_{a0} e^{-\Delta Z/Z_0 - \Delta L/L_0}, \qquad (7)$$

where $\mathbf{S}_{a0}$ is the variance of ϵ_{DSD}, ΔZ is the reflectivity difference (dBZ), Z_0 is the reflectivity scale, ΔL is the distance between pixels i and j (km), and L_0 is the length

scale. Based on the aforementioned datasets, a length scale of 10 km and reflectivity scale of 3 dBZ is used for ϵ_{DSD} and, lacking sufficient observations for independent determinations, also assumed for ϵ_{ICE} and ϵ_{CLW}.

There is less observational evidence for constraining ϵ_{ICE} than ϵ_{DSD}, but a slightly larger value (50%) is sufficient to match nearly all 85-GHz brightness temperatures with reasonable mass continuity within the column. It is likely that some snow–ice may fall below the PR detection threshold and still slightly depress 85-GHz brightness temperatures, which may lead to a low bias in retrievals of ϵ_{ICE}. This problem is effectively minimized by increasing $\mathbf{S_y}$ at 85 GHz.

The value chosen to represent the variance of ϵ_{CLW} is especially important, because rainwater and cloud water produce similar radiometric signatures, making it easy (with respect to minimizing χ^2) to adjust one at the expense of the other. However, if the rainwater content is known, then the variance in ϵ_{CLW} can be set indirectly. This approach is used in section 3.

The observation covariance ($\mathbf{S_y}$) matrices contain the measurement and modeling errors. In addition to the previously described PIA uncertainty, $\mathbf{S_y}$ represents the expected error in the brightness temperatures. This is considered to come from three sources: error in non-retrieved parameters, instrument noise, and radiative transfer model approximations. The first term is calculated by perturbing the nonretrieved parameters (SST by ±0.7 K, column water vapor by ±4 mm, wind by ±1.5 m s^{-1} following Elsaesser and Kummerow 2008) in each pixel and convolving the perturbations to TMI resolution. Typical values of these errors range from 2 to 4 K, depending on channel and rain coverage. Instrument noise is much smaller, approximately 0.5 K (Kummerow et al. 1998), and is also added to the error estimate. If the sum of these is less than 3 K, then the variance is increased to 3 K to account for radiative transfer model error (Kummerow 1993). Higher minimum values of 5 K at 37 GHz, and 20% of the T_b depression from 280 K at 85 GHz, are used to account for errors in ice particle modeling as well.

Some hard limits are also set to prevent the profiling algorithm from retrieving unphysical profiles. A lower limit of either 0.3 or the minimum value necessary to perform the Hitschfeld–Bordan adjustment to the surface is set on ϵ_{DSD} in reliable PIA pixels, and a lower limit that produces a maximum of 4 dB of attenuation is set in unreliable PIA pixels. This represents the maximum PIA that might be regarded as unreliable by the 2A21 algorithm (Meneghini et al. 2000) over ocean. Meanwhile, the upper limit on ϵ_{DSD} is set to 3.0, to prevent unrealistically large raindrops from being retrieved. The limits of ϵ_{ICE} are set at 0.2 and 4.0, mainly prevent unphysical mass

concentrations. The cloud water limits are set from 1% of the original value to a maximum LWP of 10 kg m^{-2}, based upon autoconversion thresholds in a high-aerosol environment (Liu and Daum 2004).

For computational simplicity and continuity with operational algorithms, a modified plane-parallel Eddington approximation along the TMI slant path is used to calculate the upwelling microwave radiances in this particular study, although the overall framework is constructed so that interchangeability with other radiative transfer schemes is possible. The extinction, bulk scattering, and asymmetry properties of rain, snow, graupel, and melting hydrometeor size distributions are computed using Mie theory and stored in lookup tables. Like the radiative transfer model, these tables can be easily interchanged with others, such as those generated from T-matrix or discrete dipole approximations of the hydrometeors that would more realistically simulate scattering properties at multiple frequencies and are thus particularly needed for GPM.

Using Newton's method to evaluate the nonlinear solution to minimize the cost function [Eq. (2)] requires a number of computationally intensive steps, which have different scaling relationships with the number of raining pixels n. The calculation of the Jacobian matrix ($\mathbf{K}$) requires a run of the profiling algorithm with perturbed values of ϵ_{DSD}, ϵ_{ICE}, and ϵ_{CLW} for each PR pixel, followed by calculation of the brightness temperatures and convolution to TMI resolution. While these steps are complex, they scale somewhere between $O(n)$ and $O(n^2)$.

The inversion of the $\mathbf{S_x}$ covariance matrix in Eq. (2), meanwhile, takes $O(n^3)$ time steps to compute, and for large scenes becomes the limiting step in the retrieval. As a result of these scaling relationships, an orbit must be broken up into segments to process in real time or better on current hardware. The definition of an orbit segment is somewhat arbitrary but needs to be larger than a single 10-GHz FOV, and preferably, contain several such FOVs in order to take advantage of that channel's sensitivity to heavy rain. Conversely, a segment should not be so large that, when filled with rain, the simultaneous retrieval of two parameters (ϵ_{DSD} and ϵ_{CLW}) results in prohibitive computation time. For simplicity, a segment size of 49 × 49 PR pixels was chosen for comparison with ground validation sites in section 3. For full orbits, a scheme that identifies continuous areas of rain as the segments may be a workable approach.

d. Sensitivity and information content

A particularly interesting outcome of this retrieval is the partitioning of rain and cloud water. This partitioning has always been either an explicit or implicit assumption
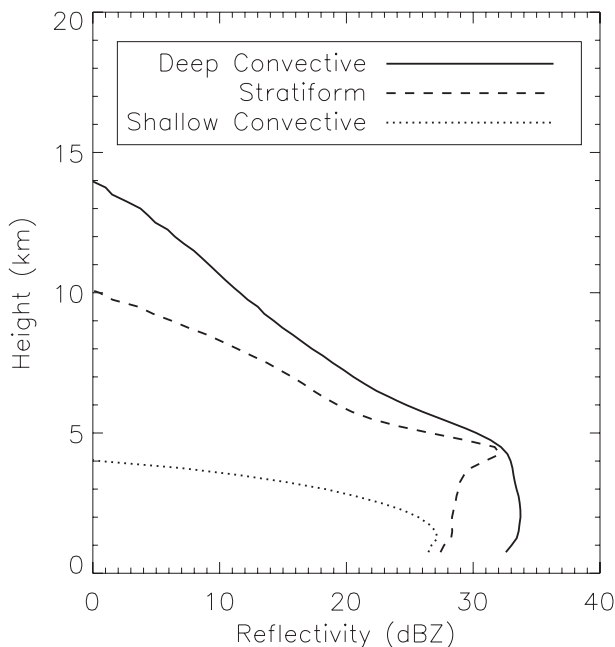
FIG. 5. Composite reflectivity profiles used in sensitivity analysis.

in the TRMM 2A12 and 2A25 products, thus this retrieval offers additional insight by retrieving it directly. However, it is first useful to evaluate the extent to which the two variables can be determined from the measurements.

We consider three reflectivity profiles which are a PR composites of stratiform, deep convective, and shallow convective rain types near Kwajalein in 2008 (Fig. 5). The ϵ_{DSD} and ϵ_{CLW} parameters were perturbed to produce a wide range of rain and cloud LWPs for each reflectivity profile, along with the associated T_bs. Given an uncertainty in the observations (i.e., $\mathbf{S_y}$), we can then determine their constraint on the physical parameters. For each profile, the difference between the perturbed and default T_bs and PIA was normalized by standard deviations of 3 K and 0.7 dB, respectively, and are plotted in Fig. 6.

The constraint provided by PIA is poor in these profiles, which is not unexpected as they are composites of all rainfall, which skews toward light rain (only the deep convective profile barely exceeds 30 dBZ). The constraint provided by the T_bs is much narrower than that provided by the PIA. Although this represents an ideal scenario, that is, uniform rain within same-size FOVs, there is clearly some additional information present in the microwave radiances. Also note that the slope of the region constrained by the T_bs is not parallel to contours of constant total LWP, but instead represents a stronger response to rainwater than cloud water, a consequence of the increased absorption efficiency of raindrops relative
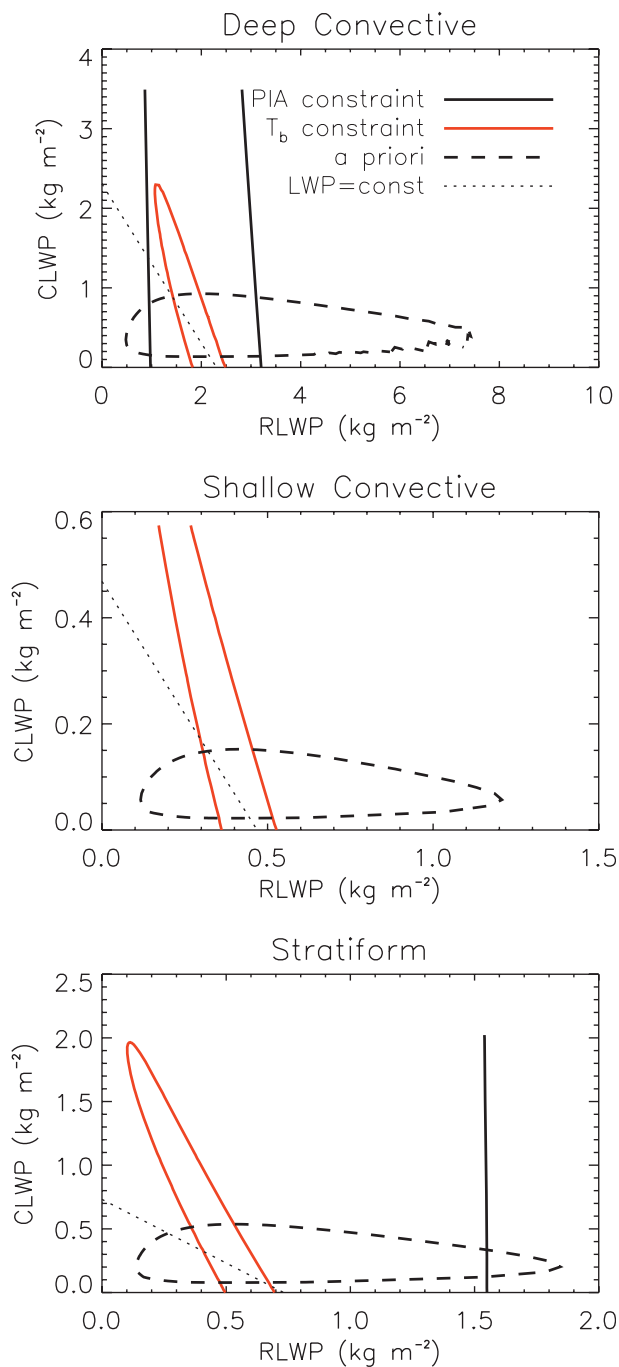

FIG. 6. Contours of the cost function for various constraint for each sample profile. The light dotted line follows the default value of total liquid water path: (top) deep convective, (middle) shallow convective, and (bottom) stratiform.

to a distribution of cloud droplets with the same liquid water content due to Mie effects.

A similar exercise is performed to examine the sensitivity of the retrieval to ice water path (IWP) and

snow–graupel partitioning. Only the deep convective and stratiform profiles are examined here since no ice is present in the shallow convective profile; however, reflectivities were increased by 10 dBZ for each profile in order to create a significant ice scattering signature. The 85V T_bs are contoured in IWP–graupel fraction space in Fig. 7, with the lines enclosing the region defined by the default T_bs $\pm$ 5 K. The most important feature of these plots is that, while T_b does vary with graupel fraction, a greater range can be achieved by altering the total IWP via ϵ_{ICE}. In some cases it may be necessary to adjust the graupel fraction to match the coldest observed T_bs, although this is not done in the current implementation.

3. Retrieval evaluation

The combined retrieval algorithm is applied to TRMM datasets within 150 km of ground radars that are part of the TRMM Ground Validation (GV) network at Melbourne, Florida, and Kwajalein, Republic of Marshall Islands (Wolff et al. 2005). These sites were selected because they represent differing precipitation regimes, significant coverage over ocean and, in addition to the standard 2-km resolution rain map (GV product 2A53), disdrometer measurements and polarimetric rainfall retrievals (Kwajalein only). The dual-polarization data from Kwajalein are used to determine the cloud water–rainwater partitioning via the uncertainty in ϵ_{CLW}, while Melbourne is used as an independent verification site. Finally, DSD statistics from ground-based disdrometers are compared to the retrievals in both locations.

a. Kwajalein

The Kwajalein Ground Validation site, located on a small atoll in the central Pacific Ocean, is an ideal site to test the combined algorithm because of its oceanic location, where the radiometer has the potential to add the most information to the radar. Although GV rain products are available since 1998, only recently have calibration problems been addressed and dual-polarization capability added (Silberstein et al. 2008; Marks et al. 2009). With these additional capabilities, a robust dataset of polarimetric rain retrievals has been developed by D. Wolff (2009, personal communication) using the method of Bringi et al. (2004).

A free parameter in the combined retrieval is the variance of ϵ_{CLW}, which determines the cloud water–rainwater partitioning. The rain probability density functions (PDFs) and cumulative distribution functions (CDFs) (Fig. 8) show that a reasonable range of uncertainty in ϵ_{CLW} provides estimates that are in line with those of the GV radar, with an optimal uncertainty of 100%. Higher values reduce the cost of changing ϵ_{CLW}, thus, the rain DSD is
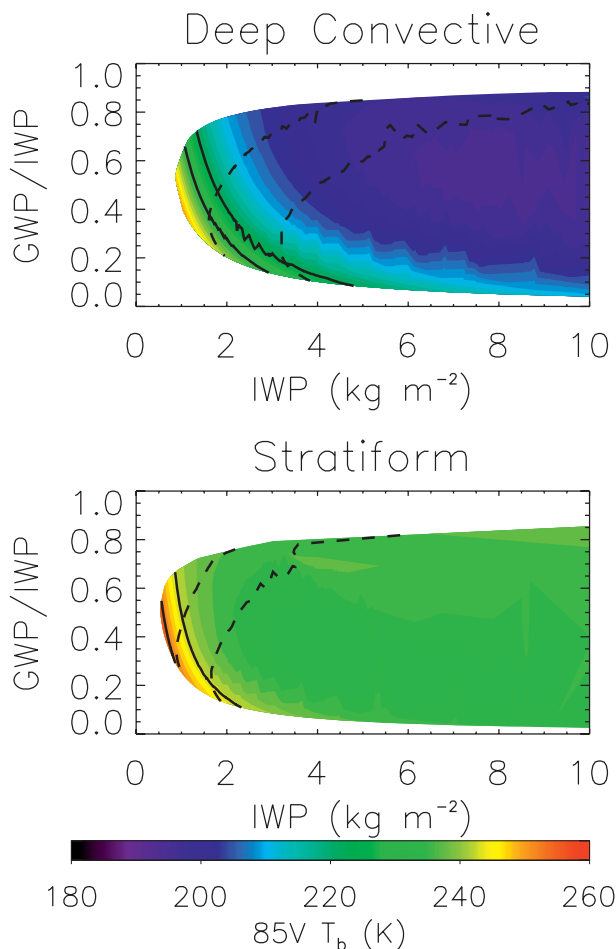

FIG. 7. Contours of the a priori (dashed) and T_b (solid) constraints as a function of graupel fraction and total IWP, overlaid on 85V T_bs: (top) deep convective and (bottom) stratiform.

modified to a lesser extent; similarly, lower values constrain cloud water more strongly, and the rain DSD is modified more readily. The GV-tuned value results in a 10% increase of rainfall over 2A25, which is in line with the PR–GV bias at Kwajalein reported by Wolff and Fisher (2008). These PDFs also show the general agreement of 2A25 and the PIA-only profiling algorithm, the low rain bias of the default DSD in this region, and general agreement of all methods in heavy rain, where the SRT measurement of PIA is most reliable.

b. Melbourne, Florida

An independent validation test was performed by comparing retrieval results to those from the standard 2A53 GV radar products over Melbourne for the years 2006–08. The mean rain rates from each retrieval are plotted in Fig. 9. It is apparent that there is much month-to-month and year-to-year variability as to which retrieval method best matches the collocated GV totals.
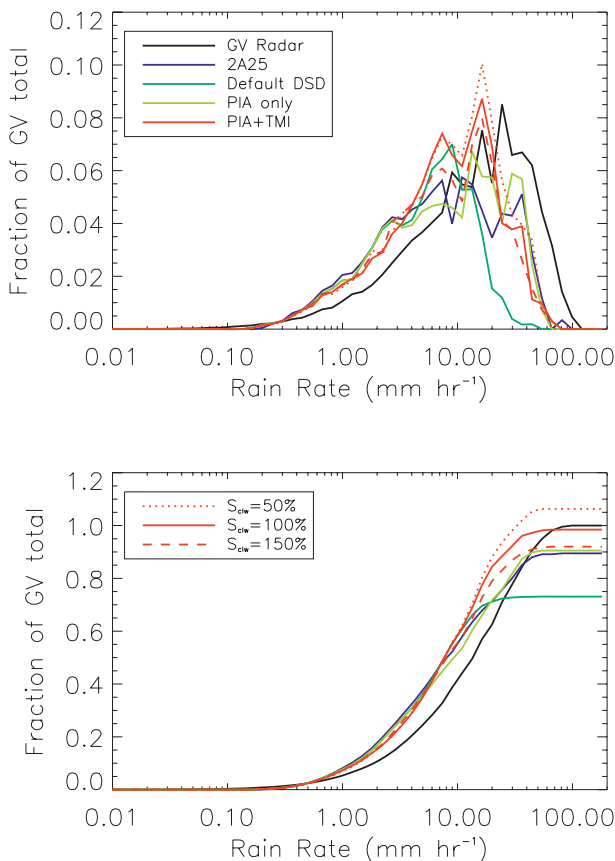
FIG. 8. (top) PDF and (bottom) CDF of near-surface rainfall rates within 110 km of the Kwajalein GV radar site during May–November 2008. The legend in the top panel refers to the retrieval method; in the bottom panel, the PIA + TMI retrieval is further divided by cloud water sensitivity. The GV radar data were not degraded to PR resolution in this figure.
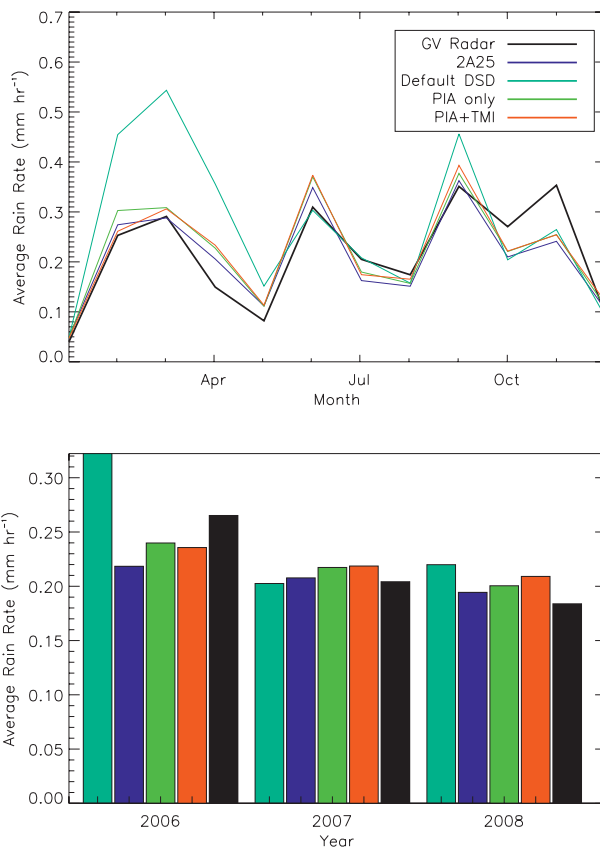
FIG. 9. (top) Monthly and (bottom) yearly mean rain rates from different retrieval methods at Melbourne, FL. Colors represent the same retrievals as in Fig. 8.

The GV Z–R relationship is based on monthly gauge accumulations, whereas there are only 10–20 overpass events each month, with just a few of these dominating the total rainfall. Thus, the average rain DSD that determines the monthly Z–R relationship may be quite different than that in the overpasses, especially considering the gauges are all on land whereas the retrievals compared here are all over the ocean. Nevertheless, the combined algorithm at the very least does no worse than the PIA-based radar algorithms in making adjustments from the default DSD. This is especially clear during January–April, when all algorithms reduce rainfall considerably relative to the default, implying larger drops as might be expected in the predominately frontal, stratiform rain that falls this time of year. The total accumulated rainfall is only 1.6% higher than GV, while 2A25 underestimates the GV total by 5% and the default DSD overestimates it by 14%. Thus, the combined method is

able to match the Melbourne rainfall while also being unbiased at Kwajalein, where 2A25 underestimates GV significantly.

c. Brightness temperature statistics

While agreement between the retrieved and observed brightness temperatures does not guarantee that correct DSD parameters are being retrieved, and cannot be considered validation in a strict sense, such internal consistency does indicate that the vertical model described in section 2 is adequate to explain the observed T_bs. Moreover, the degree to which simulated T_bs improve in the combined algorithm relative to a radar-only algorithm (such as 2A25) can also be considered a measure of the effectiveness of the retrieval.

Scatterplots of observed and simulated T_bs are shown in Fig. 10. At the lower-frequency channels it appears that a slight cold bias is evident in the default DSD and PIA-adjusted products (both 2A25 and the PIA-only version of the combined retrieval), particularly at 10 GHz. These biases are improved, but still exist to a slight degree in the
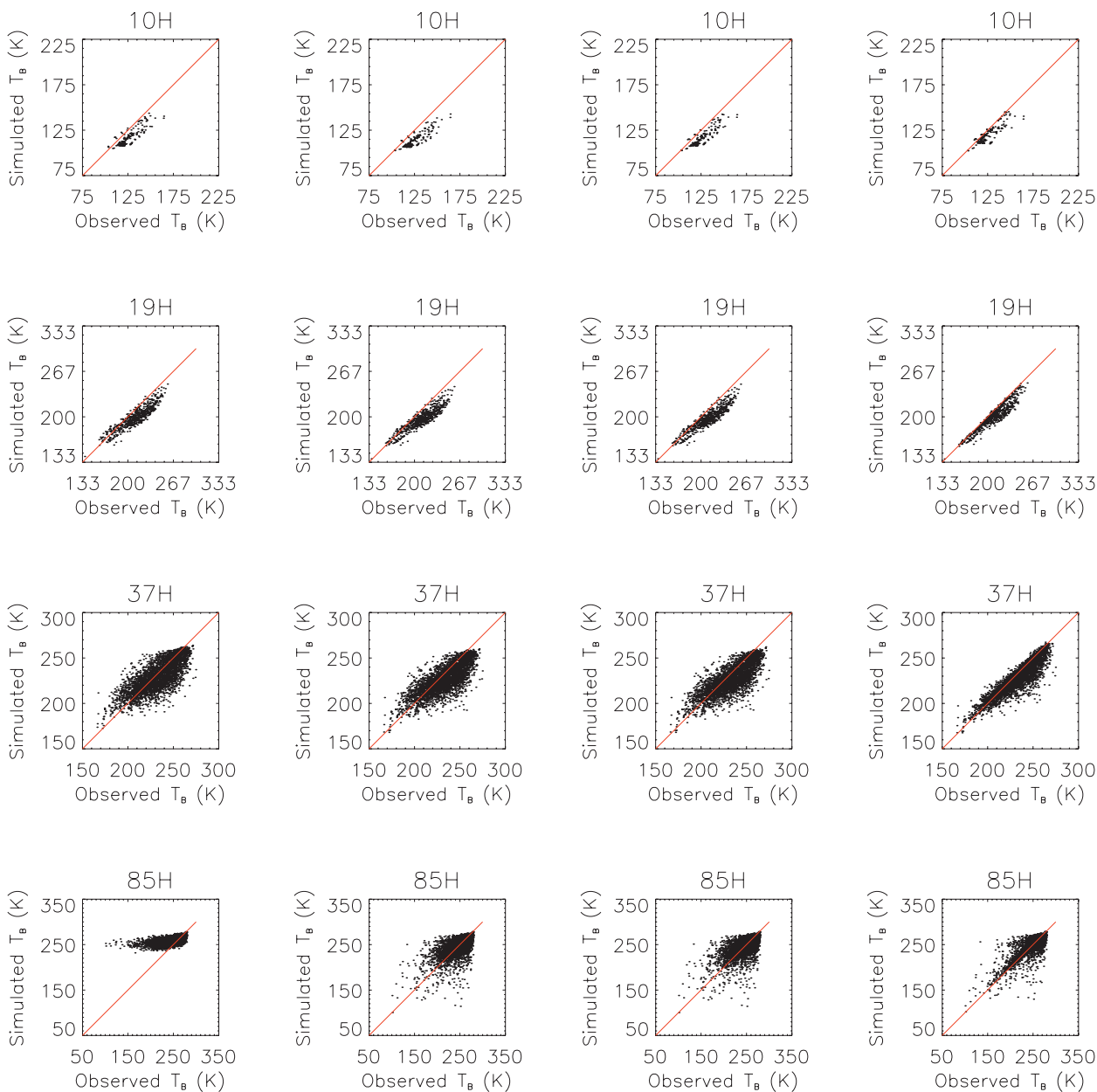
FIG. 10. Brightness temperature scatterplots for (top to bottom) 10, 19, 37, and 85 GHz.

combined product. Meanwhile, the fairly large scatter in the T_bs simulated by the radar products at 37 and 85 GHz is reduced significantly in the combined retrieval.

Quantitative measures of these errors are presented in Table 3. The largest errors and biases occur when no adjustments from the default DSD are made. When adjustments are made in heavy rain to match the PIA, errors are reduced slightly, by about 1 K, on average in the T_bs and by about 0.6 dB in the PIA. A further reduction in the T_b errors is seen with the combined algorithm but biases and RMS errors are only reduced by

about one-third to one-half of the default values, approaching the expected errors defined in the $\mathbf{S_y}$ covariance matrix. It is notable that the reduction in T_b errors has occurred without increasing the PIA errors from the radar-only algorithm. The residual RMS errors are a consequence of the OE methodology, which does not give a high value to matching observations better than the a priori error. However, the residual biases remain significant, particularly in the 19-GHz channels, and may indicate a deficiency in the forward model or calibration of these TMI channels.

TABLE 3. Brightness temperature RMS error and bias (simulated minus observed) for FOVs with at least 30% rain coverage. (In the first column, V stands for vertical polarization and H is for horizontal.)

Channel	RMS (K)				Bias (K)			
	2A25	Default	PIA only	PIA+TMI	2A25	Default	PIA only	PIA+TMI
10 GHz V	6.52	7.90	6.69	4.83	−5.70	−7.22	−6.04	−3.85
10 GHz H	10.58	12.91	10.72	7.98	−8.70	−11.46	−9.18	−5.60
19 GHz V	8.08	9.30	8.59	6.30	−6.29	−7.76	−7.16	−4.93
19 GHz H	14.17	16.12	14.85	10.89	−10.84	−13.28	−12.22	−8.37
37 GHz V	7.19	8.02	7.94	5.97	−0.77	−3.59	−3.50	−2.92
37 GHz H	13.34	13.85	13.75	9.98	−2.54	−5.91	−5.77	−4.96
85 GHz V	18.82	16.36	16.38	12.56	6.50	−2.15	−2.29	−2.83
85 GHz H	20.88	16.46	16.45	12.28	10.00	1.26	1.13	0.62
PIA (dB)	1.21	1.89	1.28	1.24	−0.38	−0.41	−0.36	−0.33

d. Disdrometer comparisons

As a final reference point, the retrieved DSDs are compared to ground-based disdrometer measurements. Because the disdrometer represents a point measurement and the number of TRMM overpasses during rain events would yield an extremely small sample size, it is more meaningful to compare summary statistics than attempt to collocate TRMM overpasses with the GV radar and disdrometer. Disdrometer data from Kwajalein are available from 2003 to 2004, and Melbourne from 2006 to 2009. Although the former do not overlap the TRMM observations we processed, the lack of a significant interannual change in DSD at Kwajalein (Kozu et al. 2009) should not prevent a statistical comparison.

Following Rosenfeld and Ulbrich (2003), we plot the liquid water content as a function of drop diameter in Fig. 11 for reflectivities representing light (20 dBZ), moderate (30 dBZ), and heavy (40 dBZ) rain. Because of errors introduced by calculating D_0 from binned disdrometer data, the mass-weighted mean diameter D_m is used instead. For a gamma distribution, assumed in both ground radar and PR retrievals, $D_m = (4 + \mu)/(3.67 + \mu)D_0$. Deviations along the lines of constant reflectivity represent changes in the DSD, going from maritime to continental as D_m increases. Deviations perpendicular to these lines represent deviations in shape parameter or from the gamma distribution itself, in the case of disdrometer data.

There is a relatively tight clustering of the DSDs derived from the TRMM data at low reflectivities that diverges as Z increases. This represents the increase in information (stronger PIA response) at higher rain rates that leads to a change from the default DSD. Curiously, the disdrometer data also show this divergence, despite the lack of any a priori assumptions in that dataset. There is also a clear increase in D_m and the decrease in W from Kwajalein to Melbourne, particularly evident in the disdrometer data, and both radar and combined retrievals. There is an apparent offset of the disdrometer data

toward larger drop sizes, which was also noted by Kozu et al. (2009) in the Kwajalein dataset, where it was suggested that noisy conditions may have contributed to an undercounting of small drops. Notwithstanding this offset, the change in D_m from Kwajalein to Melbourne is nearly identical between the combined algorithm and disdrometer at all reflectivities. This ability of the combined algorithm to distinguish DSDs is particularly evident in moderate rain where PIA-only retrievals such as 2A25 must rely on default DSD assumptions. Even the polarimetric radar algorithm Bringi et al. (2004) relies upon an assumed DSD in the lightest rain, although the small contribution of these rain rates to the total should
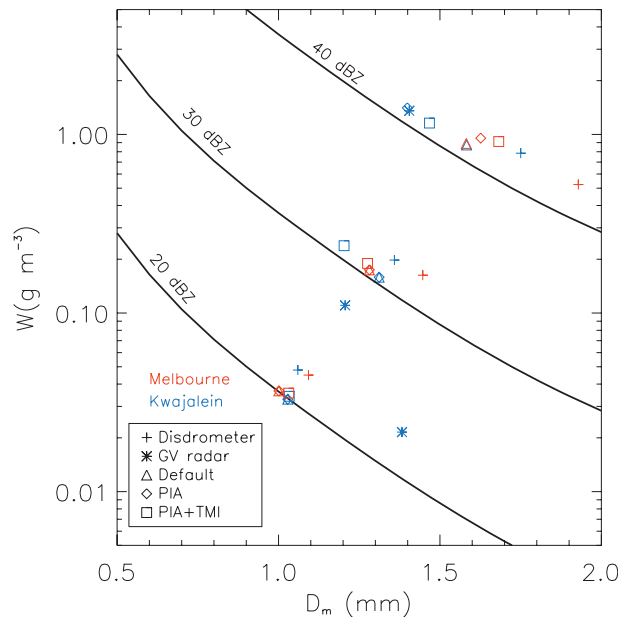

FIG. 11. Mean liquid water content W vs mean mass diameter D_m from TRMM algorithms and ground instruments at Kwajalein and Melbourne at 20-, 30-, and 40-dBZ reflectivity. The solid lines represent the theoretical relationship between W and D_m at the given reflectivity assuming a gamma distribution with $\mu = 3$.
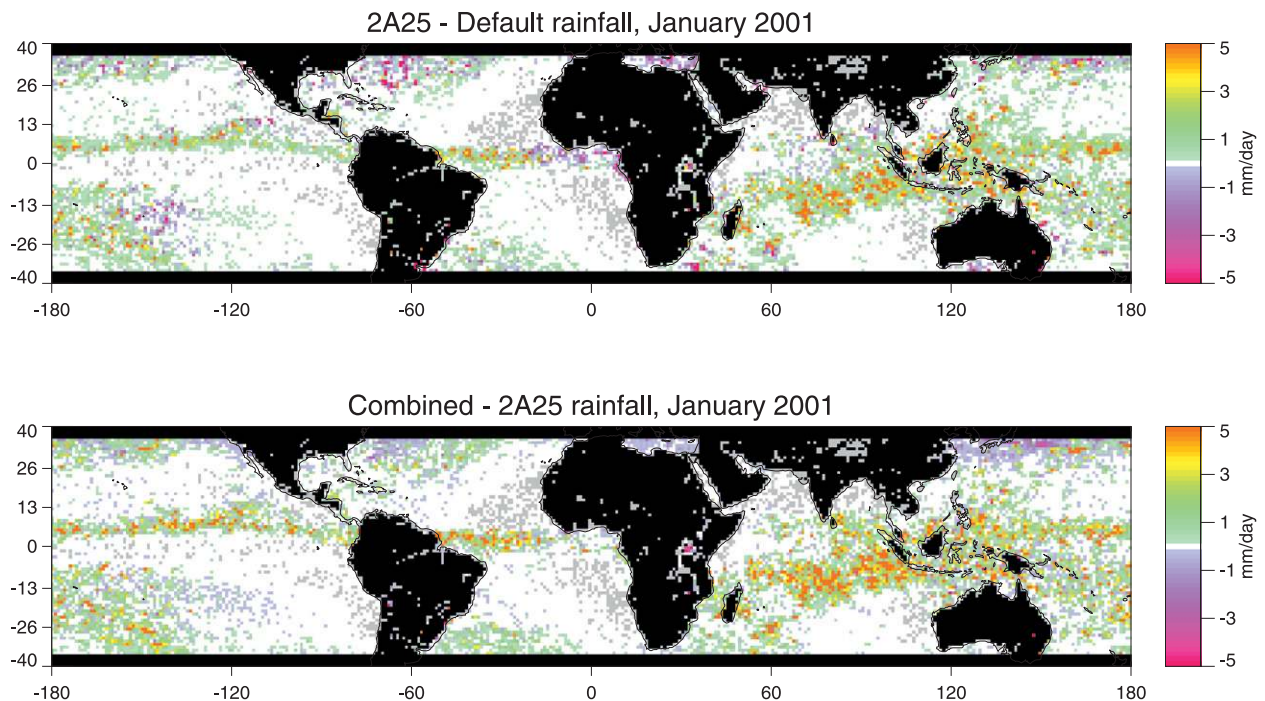
FIG. 12. Difference in mean rain rates between 2A25 and (top) the default *Z–R* relationship and (bottom) the combined and 2A25 algorithms on a 1° × 1° grid. Only the central 25 PR angle bins were analyzed to avoid biases from ground clutter and to speed computations. Black areas represent land and gray pixels represent no rain during the period.

not impact the cloud water constraint that was derived from the Kwajalein GV radar dataset.

4. Summary

Although radar- and radiometer-based satellite measurements of rainfall have been available over the global tropics for over a decade, key uncertainties remain in some regions. Instrumental strengths and shortcomings as well as algorithm assumptions are thought to play a role in creating the regional biases evident in long-term radar- and radiometer-based products from the TRMM satellite. In an effort to explain these biases as well as prepare for GPM, where combined radar–radiometer profiles will be used as the Bayesian database for constellation radiometers, a new method has been devised to use radiometer measurements to retrieve hydrometeor profiles from radar reflectivity profiles.

The key component of this method is a radar profiling algorithm with three variable parameters representing the ice PSD, rain DSD, and cloud LWP. A variational optimal estimation inversion is used to adjust the profiling algorithm parameters to best match the observed microwave radiances and SRT PIA over a scene containing hundreds to thousands of PR pixels. The overall framework is modular, allowing for easy inclusion of different microwave scattering tables and radiative transfer models

as well as any ancillary data regarding nonretrieved background parameters.

TRMM PR and ground-based radar datasets were used to set the uncertainty in the a priori DSD and cloud water assumptions. These uncertainties were fit to best match 2A25 and polarimetric radar rainfall retrievals at Kwajalein respectively. These same values were then used in retrievals over Melbourne, Florida, where rainfall totals were within 2% of the GV value, well within the range of uncertainty expected given sampling error and a significant improvement from the default DSD assumption in the winter and early spring months.

Globally, the area-weighted mean rain rate from the combined rainfall product exceeds version 6 of the 2A25 products by 17% for January 2001 (Fig. 12). Note, however, that the patterns of rainfall adjustment are nearly identical in going from the default DSD to 2A25 and 2A25 to the combined algorithm. The increase of rainfall in the combined algorithm therefore results from two sources: 1) The combined algorithm, unlike the PIA-based 2A25, is not limited to pixels with heavy rain; and 2) the majority of rainfall occurs in the regions where DSD adjustments increase rainfall. The latter of these is also evident in that the 2A25 global rainfall itself is a 14% increase over the default DSD. Nevertheless, caution is advised in interpreting the exact magnitude of this increase relative to 2A25, because it is sensitive to

the cloud water–rainwater partitioning. While the values we have selected are in good agreement with GV radar at Kwajalein and Melbourne, it is desirable to see additional confirmation elsewhere over long observation periods. Nevertheless, it does appear that some increase from version 6 of the 2A25 products is reasonable, and in fact, similar increases are seen in version 7 of the 2A25 products (J. Kwiatkowski 2010, personal communication).

A further analysis of the DSD adjustments made by the combined algorithm will be the subject of a future study. Potential areas of algorithm refinement include sensitivity analyses to different radiative transfer models and hydrometeor scattering properties, including nonspherical raindrops and more complex representations of ice. More accurate estimates of the global mean rainfall will require additional tuning of the cloud water adjustment and/or DSD assumptions using polarimetric radar data from a variety of rainfall climate regimes. To continue preparation for GPM, a dual-frequency profiling algorithm will need to be developed as well as an extension of the retrieval method over land and ice surfaces.

REFERENCES

Allen, M. R., and W. J. Ingram, 2002: Constraints on future changes in climate and the hydrologic cycle. *Nature,* **419,** 224–232.

Barrett, E. C., 1970: The estimation of monthly rainfall from satellite data. *Mon. Wea. Rev.,* **98,** 322–327.

Bennartz, R., and G. W. Petty, 2001: The sensitivity of microwave remote sensing observations of precipitation to ice particle size distributions. *J. Appl. Meteor.,* **40,** 345–364.

Berg, W., T. L'Ecuyer, and C. Kummerow, 2006: Rainfall climate regimes: The relationship of regional TRMM rainfall biases to the environment. *J. Appl. Meteor. Climatol.,* **45,** 434–454.

Black, R. A., 1990: Radar reflectivity–ice water content relationships for use above the melting level in hurricanes. *J. Appl. Meteor.,* **29,** 955–961.

Bringi, V. N., T. Tang, and V. Chandrasekar, 2004: Evaluation of a new polarimetrically based Z–R relation. *J. Atmos. Oceanic Technol.,* **21,** 612–623.

Chen, Y., A. D. D. Genio, and J. Chen, 2007: The tropical atmospheric El Niño signal in satellite precipitation data and a global climate model. *J. Climate,* **20,** 3580–3601.

Cho, H.-K., K. P. Bowman, and G. R. North, 2004: Equatorial waves including the Madden–Julian oscillation in TRMM rainfall and OLR data. *J. Climate,* **17,** 4387–4406.

Elsaesser, G. S., and C. D. Kummerow, 2008: Toward a fully parametric retrieval of the nonraining parameters over the global oceans. *J. Appl. Meteor. Climatol.,* **47,** 1599–1618.

Fabry, F., and I. Zawadzki, 1995: Long-term radar observations of the melting layer of precipitation and their interpretation. *J. Atmos. Sci.,* **52,** 838–851.

Gentemann, C. L., F. J. Wentz, C. A. Mears, and D. K. Smith, 2004: In situ validation of Tropical Rainfall Measuring Mission microwave sea surface temperatures. *J. Geophys. Res.,* **109,** C04021, doi:10.1029/2003JC002092.

Grecu, M., and E. N. Anagnostou, 2002: Use of passive microwave observations in a radar rainfall-profiling algorithm. *J. Appl. Meteor.,* **41,** 702–715.

——, W. S. Olson, and E. N. Anagnostou, 2004: Retrieval of precipitation profiles from multiresolution, multifrequency active and passive microwave observations. *J. Appl. Meteor.,* **43,** 562–575.

Haddad, Z. S., E. A. Smith, C. D. Kummerow, T. Iguchi, M. R. Farrar, S. L. Durden, M. Alves, and W. S. Olson, 1997: The TRMM 'day-1' radar/radiometer combined rain-profiling algorithm. *J. Meteor. Soc. Japan,* **75,** 799–809.

Held, I. M., and B. J. Soden, 2006: Robust responses of the hydrological cycle to global warming. *J. Climate,* **19,** 5686–5699.

Heymsfield, A. J., A. Bansemer, C. Schmitt, C. Twomey, and M. R. Poellot, 2004: Effective ice particle densities derived from aircraft data. *J. Atmos. Sci.,* **61,** 982–1003.

Hitschfeld, W., and J. Bordan, 1954: Errors inherent in the radar measurement of rainfall at attenuating wavelengths. *J. Meteor.,* **11,** 58–67.

Hollinger, J. P., J. L. Peirce, and G. A. Poe, 1990: SSM/I instrument evaluation. *IEEE Trans. Geosci. Remote Sens.,* **28,** 781–790.

Houze, R. A., P. V. Hobbs, P. H. Herzegh, and D. B. Parsons, 1979: Size distributions of precipitation particles in frontal clouds. *J. Atmos. Sci.,* **36,** 156–162.

Iguchi, T., T. Kozu, R. Meneghini, J. Awaka, and K. Okamoto, 2000: Rain-profiling algorithm for the TRMM precipitation radar. *J. Appl. Meteor.,* **39,** 2038–2052.

——, ——, J. Kwiatkowski, R. Meneghini, J. Awaka, and K. Okamoto, 2009: Uncertainties in the rain profiling algorithm for the TRMM precipitation radar. *J. Meteor. Soc. Japan,* **87A,** 1–30.

Kozu, T., T. Iguchi, T. Kubota, N. Yoshida, S. Seto, J. Kwiatkowski, and Y. N. Takayabu, 2009: Feasibility of raindrop size distribution parameter estimation with TRMM precipitation radar. *J. Meteor. Soc. Japan,* **87A,** 53–66.

Kubar, T. L., D. L. Hartmann, and R. Wood, 2009: Understanding the importance of microphysics and macrophysics for warm rain in marine low clouds. Part I: Satellite observations. *J. Atmos. Sci.,* **66,** 2953–2972.

Kummerow, C., 1993: On the accuracy of the Eddington approximation for radiative transfer in the microwave frequencies. *J. Geophys. Res.,* **98,** 2757–2765.

——, and L. Giglio, 1994: A passive microwave technique for estimating rainfall and vertical structure information from space. Part I: Algorithm description. *J. Appl. Meteor.,* **33,** 3–18.

——, W. Barnes, T. Kozu, J. Shiue, and J. Simpson, 1998: The Tropical Rainfall Measuring Mission (TRMM) sensor package. *J. Atmos. Oceanic Technol.,* **15,** 809–817.

——, and Coauthors, 2001: The evolution of the Goddard Profiling Algorithm (GPROF) for rainfall estimation from passive microwave sensors. *J. Appl. Meteor.,* **40,** 1801–1820.

L'Ecuyer, T. S., and G. L. Stephens, 2007: The tropical atmospheric energy budget from the TRMM perspective. Part II: Evaluating GCM representations of the sensitivity of regional

energy and water cycles to the 1998/99 ENSO cycle. *J. Climate,* **20,** 4548–4571.

Li, Y., E. J. Zipser, S. K. Krueger, and M. A. Zulauf, 2008: Cloud-resolving modeling of deep convection during KWAJEX. Part I: Comparison to TRMM satellite and ground-based radar observations. *Mon. Wea. Rev.,* **136,** 2699–2712.

Liu, Y., and P. H. Daum, 2004: Parameterization of the auto-conversion process. Part I: Analytical formulation of Kessler-type parameterizations. *J. Atmos. Sci.,* **61,** 1539–1548.

Marks, D. A., D. B. Wolff, D. S. Silberstein, A. Tokay, J. L. Pippitt, and J. Wang, 2009: Availability of high-quality TRMM ground validation data from Kwajalein, RMI: A practical application of the relative calibration adjustment technique. *J. Atmos. Oceanic Technol.,* **26,** 413–429.

Masunaga, H., and C. Kummerow, 2005: Combined radar and radiometer analysis of precipitation profiles for a parametric retrieval algorithm. *J. Atmos. Oceanic Technol.,* **22,** 909–929.

——, T. S. L'Ecuyer, and C. D. Kummerow, 2006: The Madden–Julian Oscillation recorded in early observations from the Tropical Rainfall Measuring Mission (TRMM). *J. Atmos. Sci.,* **63,** 2777–2794.

Matrosov, S. Y., K. Clark, B. Martner, and A. Tokay, 2002: X-band polarimetric radar measurements of rainfall. *J. Appl. Meteor.,* **41,** 941–952.

Meneghini, R., T. Iguchi, T. Kozu, L. Liao, K. Okamoto, J. A. Jones, and J. Kwiatkowski, 2000: Use of the surface reference technique for path attenuation estimates from the TRMM radar. *J. Appl. Meteor.,* **39,** 2053–2070.

Morita, J., Y. N. Takayabu, S. Shige, and Y. Kodama, 2006: Analysis of rainfall characteristics of the Madden-Julian oscillation using TRMM satellite data. *Dyn. Atmos. Oceans,* **42,** 107–126.

Olson, W. S., P. Bauer, N. F. Viltard, D. E. Johnson, W.-K. Tao, R. Meneghini, and L. Liao, 2001: A melting-layer model for passive/active microwave remote sensing applications. Part I: Model formulation and comparison with observations. *J. Appl. Meteor.,* **40,** 1145–1163.

Petty, G. W., and W. Huang, 2010: Microwave backscatter and extinction by soft ice spheres and complex snow aggregates. *J. Atmos. Sci.,* **67,** 769–787.

Rapp, A. D., M. Lebsock, and C. Kummerow, 2009: On the consequences of resampling microwave radiometer observations for use in retrieval algorithms. *J. Appl. Meteor. Climatol.,* **48,** 1981–1993.

Reynolds, R. W., and T. Smith, 1994: Improved global sea surface temperature analyses using optimum interpolation. *J. Climate,* **7,** 929–948.

Rodgers, C. D., 2000: *Inverse Methods for Atmospheric Sounding: Theory and Practice.* World Scientific, 238 pp.

Rosenfeld, D., and C. W. Ulbrich, 2003: Cloud microphysical properties, processes and rainfall estimation opportunities. *Radar and Atmospheric Science: A Collection of Essays in Honor of David Atlas, Meteor. Monogr.,* No. 52, Amer. Meteor. Soc., 237–258.

Seo, E.-K., B.-J. Sohn, and G. Liu, 2007: How TRMM precipitation radar and microwave imager retrieved rain rates differ. *Geophys. Res. Lett.,* **34,** L24803, doi:10.1029/2007GL032331.

Shimizu, S., R. Oki, T. Tagawa, T. Iguchi, and M. Hirose, 2009: Effects of the orbit boost of the TRMM satellite on PR rain estimates. *J. Meteor. Soc. Japan,* **87A,** 83–92.

Silberstein, D. S., D. B. Wolff, D. A. Marks, D. Atlas, and J. L. Pippitt, 2008: Ground clutter as a monitor of radar stability at Kwajalein, RMI. *J. Atmos. Oceanic Technol.,* **25,** 2037–2045.

Stephens, G. L., and Coauthors, 2002: The CloudSat mission and the A-Train: A new dimension of space-based observations of clouds and precipitation. *Bull. Amer. Meteor. Soc.,* **83,** 1771–1790.

Stith, J. L., J. E. Dye, A. Bansemer, A. J. Heymsfield, C. A. Grainger, W. A. Petersen, and R. Cifelli, 2002: Microphysical observations of tropical clouds. *J. Appl. Meteor.,* **41,** 97–117.

Ulbrich, C. W., 1983: Natural variations in the analytical form of the drop size distribution. *J. Climate Appl. Meteor.,* **22,** 1764–1775.

Wentz, F. J., L. Ricciardulli, K. Hilburn, and C. Mears, 2007: How much more rain will global warming bring? *Science,* **317,** 233–235.

Williams, C. R., 2008: Profiler DSD estimates and uncertainties retrieved using ensemble statistics and optimal estimation theory. *Third Int. TRMM Conf.,* Las Vegas, NV, National Aeronautics and Space Agency/Japan Aerospace Exploration Agency. [Available online at http://trmm.gsfc.nasa.gov/3rd_trmm_conf/session_9/Williams_Wed_0510pm.ppt.]

Wolff, D. B., and B. L. Fisher, 2008: Comparisons of instantaneous TRMM ground validation and satellite rain-rate estimates at different spatial scales. *J. Appl. Meteor. Climatol.,* **47,** 2215–2237.

——, D. A. Marks, E. Amitai, D. S. Silberstein, B. L. Fisher, A. Tokay, J. Wang, and J. L. Pippitt, 2005: Ground validation for the Tropical Rainfall Measuring Mission (TRMM). *J. Atmos. Oceanic Technol.,* **22,** 365–380.

Zawadzki, I., W. Szyrmer, C. Bell, and F. Fabry, 2005: Modeling of the melting layer. Part III: The density effect. *J. Atmos. Sci.,* **62,** 3705–3722.